Coiling of viscous jets

N. M. Ribe

Email alerting service	Receive free email alerts when new articles cite this article - sign up in the box at the top right-hand corner of the article or click **here**

THE ROYAL SOCIETY

Coiling of viscous jets

By Neil M. Ribe

CNRS UMR 7579, Institut de Physique du Globe, 4 place Jussieu, 75252 Paris CEDEX 05, France (ribe@ipgp.jussieu.fr)

A stream of viscous fluid falling from a sufficient height onto a surface forms a series of regular coils. I use a numerical model for a deformable fluid thread to predict the coiling frequency as a function of the thread's radius, the flow rate, the fall height, and the fluid viscosity. Three distinct modes of coiling can occur: viscous (e.g. toothpaste), gravitational (honey falling from a moderate height) and inertial (honey falling from a great height). When inertia is significant, three states of steady coiling with different frequencies can exist over a range of fall heights. The numerically predicted coiling frequencies agree well with experimental measurements in the inertial coiling regime.

Keywords: viscous jet; buckling instability; fluid rope coiling

1. Introduction

The periodic buckling of a fluid jet incident on a surface is a striking fluid mechanical instability with applications from food processing (Tome & McKee 1999) to polymer processing (Pearson 1985) and geophysics (Griffiths & Turner 1988). Its most beautiful manifestation is the 'fluid rope-coil' effect that occurs when a thin stream of honey is poured onto toast (figure 1a). Fluid coiling has been studied extensively in the laboratory for nearly 50 years (Barnes & Woodcock 1958; Barnes & MacKenzie 1959; Cruickshank 1980; Cruickshank & Munson 1981; Huppert 1986; Griffiths & Turner 1988; Mahadevan *et al.* 1998). However, its mechanism remains incompletely understood. The first important theoretical advance was Taylor's recognition that fluid buckling requires a longitudinal compressive stress, like the buckling of an elastic column under a load (Taylor 1968). Subsequently, the critical fall height and frequency at the onset of coiling were determined using linear stability analysis (Cruickshank 1988; Tchavdarov *et al.* 1993). Most recently, Mahadevan *et al.* (1998, 2000) proposed a scaling law for inertia-dominated coiling that agreed well with experimental measurements in the high-frequency limit.

In summary, current theoretical understanding of fluid coiling is limited to the extremes of very low (incipient coiling) and very high (inertial coiling) frequencies. Here I use a numerical approach to model coiling over the whole frequency range, and to document the existence of three distinct coiling modes with different dynamics. The configuration studied is the one used in most laboratory experiments, where fluid with density ρ and kinematic viscosity ν is injected at a volumetric rate Q through a hole of radius a_0 and falls a distance H onto a plate (figure 1a). For simplicity I shall neglect surface tension, which has only a small (at most a few per cent) effect on
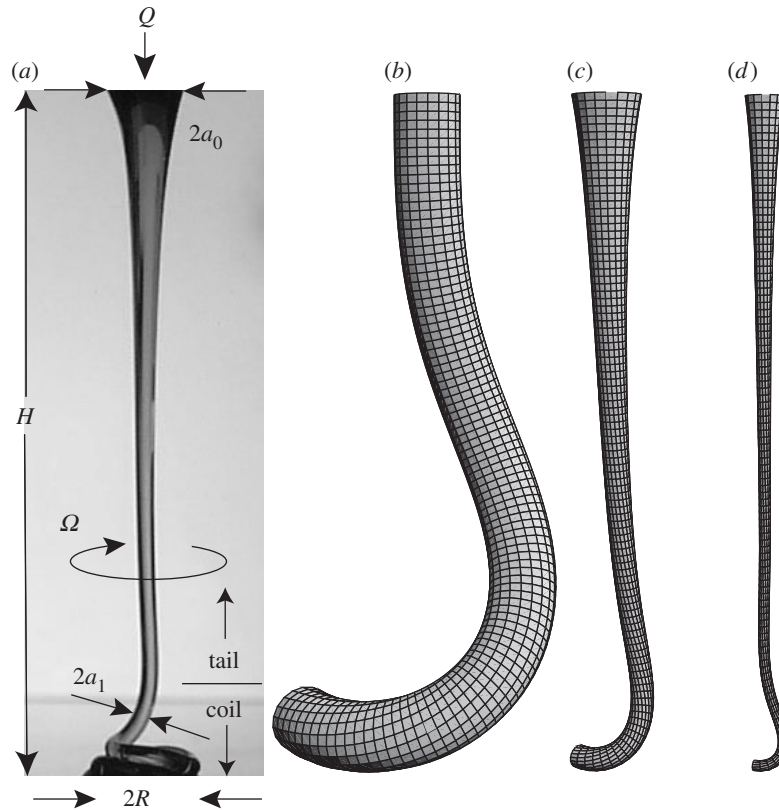
Figure 1. Modes of fluid coiling. (a) Coiling of a jet of viscous corn syrup (photograph by the author), showing the parameters of a typical laboratory experiment. (b)–(d) Jet shapes calculated using Auto97 (Doedel *et al.* 2002) for three modes of fluid coiling. (b) Viscous coiling ($H/a_0 = 20$, $B \equiv gH^2/\nu U_0 = 0$, $Re \equiv U_0 H/\nu = 0$). (c) Gravitational coiling ($H/a_0 = 20$, $B = 100$, $Re = 0$). (d) Inertial coiling ($H/a_0 = 37$, $B = 164$, $Re = 0.031$).

the coiling frequency. The jet's point of contact with the plate rotates with angular velocity Ω and describes a circle of radius R. In most cases, the jet consists of a long, nearly vertical 'tail' which feeds fluid to a 'coil' next to the plate.

This study is based on equations that describe the dynamics of a thin viscous jet whose 'slenderness' $\epsilon \equiv a\kappa \ll 1$, where a and κ are characteristic values of the jet's radius and axial curvature, respectively. The equations governing the steady coiling of such a jet are derived in § 2, where it is shown that the phenomenon is described by a 17th-order nonlinear two-point boundary-value problem with two free parameters and 19 boundary conditions. The numerical solution of these equations is explained in § 3. Readers uninterested in the details of the derivation may skip directly to the presentation of the results in § 4.

2. Governing equations for steady coiling

The essential goal of the derivation that follows is to exploit the jet's slenderness to reduce the three-dimensional Navier–Stokes equations to one-dimensional equations that describe the dynamics of a curved line (the jet axis) endowed with finite resis-
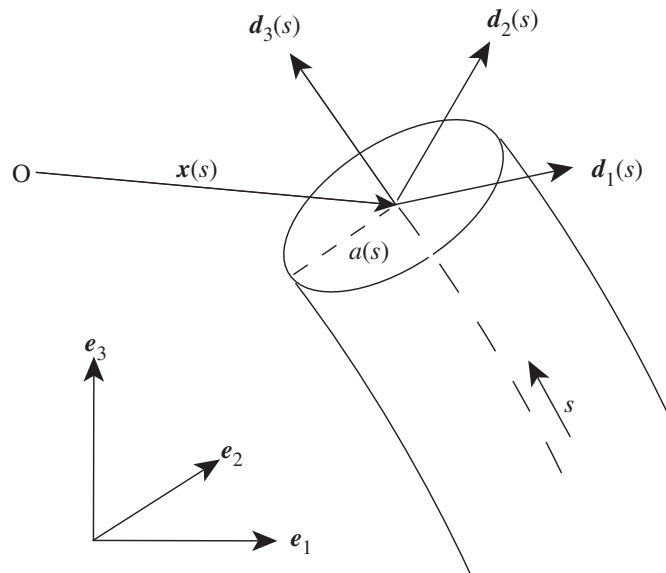
Figure 2. Geometry of a viscous jet. The Cartesian coordinates of the jet's axis relative to an arbitrary origin, O, are $\boldsymbol{x}(s)$, where s is the arc length along the axis. The jet's radius is $a(s)$. The unit tangent vector to the jet axis is $\boldsymbol{d}_3(s) \equiv \boldsymbol{x}'$, and $\boldsymbol{d}_1(s)$ and $\boldsymbol{d}_2(s) \equiv \boldsymbol{d}_3 \times \boldsymbol{d}_1$ are material unit vectors in the plane of the jet's cross-section.

tance to stretching, bending and twisting. The problem is further reduced to one of steady motion by working in a reference frame that rotates with the coil. All the dependent variables are then functions only of the arc length s along the jet axis, which ranges from $s = 0$ (the injection point) to $s = \ell$ (the unknown point of contact with the plate).

In the following, differentiation with respect to s will be denoted by a prime. Unless otherwise noted, all Latin indices range over the values 1, 2 and 3, while Greek indices range over 1 and 2 only. The Einstein summation convention over repeated indices (both Latin and Greek) is assumed throughout.

Figure 2 shows an element of a slender viscous jet with variable radius $a(s)$. The Cartesian coordinates of the jet's axis relative to unit vectors $\boldsymbol{e}_i$ rotating with the coil are $\boldsymbol{x}(s)$, defined such that $(x_1, x_2, x_3) = (0, 0, 0)$ is the point where the fluid is injected. The vector $\boldsymbol{e}_3$ points up, opposite to the gravitational acceleration $\boldsymbol{f} \equiv -g\boldsymbol{e}_3$. At each point on the jet's axis, a triad of orthogonal unit vectors is defined, comprising the tangent vector $\boldsymbol{d}_3(s) \equiv \boldsymbol{x}'$ and two vectors $\boldsymbol{d}_1(s)$ and $\boldsymbol{d}_2(s) \equiv \boldsymbol{d}_3 \times \boldsymbol{d}_1$ in the plane of the jet's cross-section. The vectors $\boldsymbol{d}_1$ and $\boldsymbol{d}_2$ are arbitrary, but are assumed to be material vectors that rotate with the fluid. An alternative approach in which $\boldsymbol{d}_1$ and $\boldsymbol{d}_2$ are defined geometrically as the principal normal and binormal of the jet axis (Entov & Yarin 1984) leads in my experience to equations that are numerically unstable when the total curvature of the axis is small. Let y_1 and y_2 be orthogonal coordinates normal to the jet axis in the directions $\boldsymbol{d}_1$ and $\boldsymbol{d}_2$, respectively. The Cartesian coordinates of an arbitrary point within the jet are then

$$\boldsymbol{r}(s, y_1, y_2) = \boldsymbol{x}(s) + y_1 \boldsymbol{d}_1(s) + y_2 \boldsymbol{d}_2(s) \equiv \boldsymbol{x} + \boldsymbol{y}. \tag{2.1}$$

The orientation of the local basis vectors relative to the Cartesian basis is described by the matrix of direction cosines

$$d_{ij} \equiv \boldsymbol{d}_i \cdot \boldsymbol{e}_j = \begin{bmatrix} q_1^2 - q_2^2 - q_3^2 + q_0^2 & 2(q_1 q_2 + q_0 q_3) & 2(q_1 q_3 - q_0 q_2) \\ 2(q_1 q_2 - q_0 q_3) & -q_1^2 + q_2^2 - q_3^2 + q_0^2 & 2(q_2 q_3 + q_0 q_1) \\ 2(q_1 q_3 + q_0 q_2) & 2(q_2 q_3 - q_0 q_1) & -q_1^2 - q_2^2 + q_3^2 + q_0^2 \end{bmatrix}, \quad (2.2)$$

where $q_i(s)$ are Euler parameters (Whittaker 1944) satisfying

$$q_0^2 + q_1^2 + q_2^2 + q_3^2 = 1. \quad (2.3)$$

Use of the Euler parameters avoids the polar singularities associated with the more familiar Eulerian angles. The ordinary differential equations satisfied by x_i and q_j are (Mahadevan & Keller 1996)

$$x_i' = d_{3i}, \quad (2.4)$$

$$\left.\begin{aligned} q_0' &= \tfrac{1}{2}(-\kappa_1 q_1 - \kappa_2 q_2 - \kappa_3 q_3), \\ q_1' &= \tfrac{1}{2}(\kappa_1 q_0 - \kappa_2 q_3 + \kappa_3 q_2), \\ q_2' &= \tfrac{1}{2}(\kappa_1 q_3 + \kappa_2 q_0 - \kappa_3 q_1), \\ q_3' &= \tfrac{1}{2}(-\kappa_1 q_2 + \kappa_2 q_1 + \kappa_3 q_0), \end{aligned}\right\} \quad (2.5)$$

where $\boldsymbol{\kappa} \equiv \kappa_i \boldsymbol{d}_i$ is the curvature vector that measures the rates of change of the local basis vectors along the jet axis according to the generalized Frenet relations

$$\boldsymbol{d}_i' = \boldsymbol{\kappa} \times \boldsymbol{d}_i. \quad (2.6)$$

To first order in the lateral coordinates y_1 and y_2, the velocity of a fluid particle in the jet relative to the rotating reference frame is

$$\boldsymbol{u} = U \boldsymbol{d}_3 - \tfrac{1}{2} U' \boldsymbol{y} + \boldsymbol{\omega} \times \boldsymbol{y}, \quad (2.7)$$

where

$$\boldsymbol{\omega} = \kappa_1 U \boldsymbol{d}_1 + \kappa_2 U \boldsymbol{d}_2 + \omega_3 \boldsymbol{d}_3 \quad (2.8)$$

is one-half the vorticity at the jet axis $y_1 = y_2 = 0$, $U(s)\boldsymbol{d}_3(s)$ is the velocity along the axis, and $\omega_3(s)$ is the angular velocity (spin) of the fluid about the axis. The second term on the right-hand side of (2.7) is the lateral velocity induced by stretching of the axis at a rate U'. The third term represents the velocity associated with bending and twisting of the jet.

Because the base vectors $\boldsymbol{d}_i$ are convected with the fluid, their angular velocity as they travel along the jet axis is the sum of the angular velocity $\boldsymbol{\omega}$ of the flow and any additional spin that is imparted to the vectors $\boldsymbol{d}_1$ and $\boldsymbol{d}_2$ when they are injected at $s = 0$. Now $\boldsymbol{d}_1$ and $\boldsymbol{d}_2$ can only be steady in the rotating frame if they are injected at $s = 0$ in such a way as to follow the rotation of the jet as a whole. This is equivalent to imparting to $\boldsymbol{d}_1$ and $\boldsymbol{d}_2$ and additional spin of magnitude $-\Omega$, where the minus sign accounts for the fact that $\boldsymbol{e}_3$ points up and $\boldsymbol{d}_3(0)$ down. The evolution equation for $\boldsymbol{d}_i$ is therefore

$$U \boldsymbol{d}_i' = (\boldsymbol{\omega} - \Omega \boldsymbol{d}_3) \times \boldsymbol{d}_i, \quad (2.9)$$

where the left-hand side is the (steady) convective rate of change of $\boldsymbol{d}_i$ along the jet axis. Substitution of the Frenet relations (2.6) into (2.9) yields the fundamental condition for the steadiness of $\boldsymbol{d}_i(s)$:

$$\kappa_3 = U^{-1}(\omega_3 - \Omega). \quad (2.10)$$

Equation (2.10) allows κ_3 to be eliminated from all the equations that follow.

Equations for the global balance of force and torque on the jet are obtained by integrating the Navier–Stokes equations over the jet's cross-section S (Appendix A). The dynamical variables that then appear are the stress resultant vector

$$\boldsymbol{N} \equiv N_i \boldsymbol{d}_i = \int_S \boldsymbol{\sigma} \, \mathrm{d}S \tag{2.11}$$

and the bending/twisting moment vector

$$\boldsymbol{M} \equiv M_i \boldsymbol{d}_i = \int_S \boldsymbol{y} \times \boldsymbol{\sigma} \, \mathrm{d}S, \tag{2.12}$$

where $\boldsymbol{\sigma}$ is the stress vector acting on the jet's cross-section. The quantities N_3, M_1, M_2 and M_3 measure the jet's resistance to stretching, bending in two orthogonal directions, and twisting, respectively. The resultants N_1 and N_2 are the integrals of the shear stresses that accompany bending and twisting, and are generally small.

The integrated balance of forces per unit jet length is (Appendix A)

$$\rho A[\boldsymbol{\Omega} \times (\boldsymbol{\Omega} \times \boldsymbol{x}) + 2\boldsymbol{\Omega} \times \boldsymbol{U} + U\boldsymbol{U}'] = \boldsymbol{N}' + \rho A \boldsymbol{f}, \tag{2.13}$$

where $A(s) \equiv \pi a(s)^2$ is the area of the jet's cross-section. The two terms on the right-hand side represent the viscous force that resists deformation of the jet and the force of gravity, respectively. The three inertial terms on the left-hand side represent the centrifugal force, the Coriolis force and the accelerations due to variations in the axial velocity $\boldsymbol{U} \equiv U\boldsymbol{d}_3$, respectively.

The integrated torque balance is

$$\rho I \boldsymbol{K} = \boldsymbol{M}' + \boldsymbol{d}_3 \times \boldsymbol{N} + \rho I[(\boldsymbol{f} \times \boldsymbol{d}_3)\boldsymbol{\kappa} - (\boldsymbol{\kappa} \times \boldsymbol{f})\boldsymbol{d}_3], \tag{2.14}$$

where and $I \equiv \pi a^4/4$ is the moment of inertia of the jet's cross-section and the components of $\boldsymbol{K} \equiv K_i \boldsymbol{d}_i$ are

$$K_\alpha = U(U\kappa_\alpha)' - \Omega U' d_{\alpha 3} - \Omega^2 \kappa_\alpha d_{3\beta} x_\beta$$
$$+ \epsilon_{\alpha\beta3}[\Omega d_{\beta3}(\Omega d_{33} + 2\omega_3) + U\kappa_\beta(\Omega + \omega_3)], \tag{2.15a}$$
$$K_3 = 2U\omega_3' - 2U'(\Omega d_{33} + \omega_3) + \Omega^2 \kappa_\alpha d_{\alpha\beta} x_\beta + 4\epsilon_{\alpha\beta3}\Omega U d_{\alpha3}\kappa_\beta. \tag{2.15b}$$

Four additional differential equations appear in the form of constitutive relations for the stress resultant N_3 and the moments M_1, M_2, and M_3. The derivation outlined in Appendix B yields

$$N_3 = 3\mu A U', \tag{2.16a}$$
$$M_1 = 3\mu I[(U\kappa_1)' + \kappa_2(\omega_3 - \kappa_3 U)], \tag{2.16b}$$
$$M_2 = 3\mu I[(U\kappa_2)' - \kappa_1(\omega_3 - \kappa_3 U)], \tag{2.16c}$$
$$M_3 = 2\mu I\omega_3', \tag{2.16d}$$

where $\mu \equiv \rho\nu$ is the dynamic viscosity. Finally, the system of equations is closed by eliminating the jet radius a using the volume flux conservation relation

$$\pi a^2 U = Q. \tag{2.17}$$

Equations (2.4), (2.5), (2.13), (2.14) and (2.16) are a system of 17 first-order differential equations for the 17 variables x_1, x_2, x_3, q_0, q_1, q_2, q_3, κ_1, κ_2, U, ω_3,

N_1, N_2, N_3, M_1, M_2 and M_3. However, there are also two unknown parameters (Ω and ℓ), so 19 boundary conditions are required. Defining the point of injection as the origin yields the three conditions

$$x_1(0) = x_2(0) = x_3(0) = 0. \tag{2.18}$$

The jet is injected vertically downward, which requires $d_{33}(0) = -1$ or

$$q_0(0) = q_3(0) = 0. \tag{2.19}$$

The vanishing of the rotation rate of the tangent vector $\boldsymbol{d}_3$ at the point of injection requires

$$\kappa_1(0) = \kappa_2(0) = 0. \tag{2.20}$$

The velocity of injection is U_0, or

$$U(0) = U_0. \tag{2.21}$$

If the jet is extruded without rotation in the laboratory frame, its apparent rate of rotation viewed in the rotating frame (noting that $\boldsymbol{e}_3$ points up and $\boldsymbol{d}_3(0)$ down) is

$$\omega_3(0) = \Omega. \tag{2.22}$$

Consider now the contact point $s = \ell$, which may be supposed, without loss of generality, to lie on the positive x_1 axis in the rotating frame, so that

$$x_2(\ell) = 0. \tag{2.23}$$

Contact of the jet with the plate requires

$$x_3(\ell) = -H + a(\ell). \tag{2.24}$$

The values of the Euler parameters at $s = \ell$ can be found by noting that the contact point can move only if both the tangent and the principal normal to the jet axis are horizontal there, or

$$d_{33}(\ell) = \kappa_2(\ell)d_{13}(\ell) - \kappa_1(\ell)d_{23}(\ell) = 0. \tag{2.25}$$

Without loss of generality we may take $\boldsymbol{d}_1(\ell)$ to be the principal normal, which points in the $-\boldsymbol{e}_1$ direction (toward the centre of the coil). Moreover, the tangent vector $\boldsymbol{d}_3(\ell)$ points in the $-\boldsymbol{e}_2$ direction, implying $d_{32}(\ell) = d_{23}(\ell) = d_{11}(\ell) = -1$. Accordingly, the moving contact line conditions (2.25) are satisfied if

$$q_0(\ell) = q_1(\ell) = q_2(\ell) - 2^{-1/2} = q_3(\ell) + 2^{-1/2} = 0 \tag{2.26}$$

and

$$\kappa_1(\ell) = 0. \tag{2.27}$$

The contact point traces out a circle with radius $1/\kappa_2(\ell)$, implying

$$x_1(\ell)\kappa_2(\ell) = 1. \tag{2.28}$$

The no-slip condition at the contact point implies that the jet cannot rotate about its axis, or

$$\omega_3(\ell) = 0. \tag{2.29}$$

Finally, the axial fluid velocity at the contact point must equal the velocity of the contact itself, or

$$\kappa_2(\ell)U(\ell) = \Omega. \tag{2.30}$$

Equations (2.18)–(2.24) and (2.26)–(2.30) are the 19 boundary conditions required.

3. Numerical solution

I solve the above two-point boundary-value problem numerically using the program AUTO97 (Doedel *et al.* 2002). This program implements an automatic continuation (homotopy) method, wherein a simple analytical solution of the governing equations is gradually adjusted until it satisfies all the boundary conditions. The starting point is the following analytical solution of the equations for a (non-coiling) jet having the form of a quarter circle in the absence of gravity and inertia:

$$\left. \begin{aligned} \Omega = 0, \qquad \ell = \tfrac{1}{2}\pi H, \\ x_1 = H\left(1 - \cos\frac{\pi s}{2\ell}\right), \qquad x_3 = -H\sin\frac{\pi s}{2\ell}, \\ q_1 = -\cos\frac{\pi s}{4\ell}, \qquad q_3 = -\sin\frac{\pi s}{4\ell}, \qquad \kappa_2 = H^{-1}, \qquad U = U_0, \\ x_2 = q_0 = q_2 = \kappa_1 = \omega_3 = N_1 = N_2 = N_3 = M_1 = M_2 = M_3 = 0. \end{aligned} \right\} \tag{3.1}$$

The above solution satisfies all but five of the boundary conditions. Accordingly, I rewrite these conditions by adding continuation parameters c_i ($i = 1, \ldots, 5$), as follows:

$$\begin{aligned} 0 &= H\kappa_2(0) - 1 + c_1 \\ &= H\kappa_2(\ell)U(\ell) - U_0 + c_2(U_0 - H\Omega) \\ &= x_3(\ell) + H - c_3 a(\ell) \\ &= q_0(\ell) - 2^{-1/2}\cos\phi_+ = q_1(\ell) - 2^{-1/2}\sin\phi_- \\ &= q_2(\ell) - 2^{-1/2}\cos\phi_- = q_3(\ell) - 2^{-1/2}\sin\phi_+, \end{aligned} \tag{3.2}$$

where

$$\phi_\pm = \tfrac{1}{4}\pi(c_4 \mp c_5 - 2). \tag{3.3}$$

The analytical solution (3.1) satisfies the boundary conditions (3.2) with $c_i = 0$, while the boundary conditions for the full coiling problem are obtained when $c_i = 1$. Beginning from the analytical solution with $c_i = 0$, the numerical procedure consists in gradually increasing the c_i until a solution of the full coiling problem is reached. This solution is then continued further by adding gravity and inertia terms.

Before numerical solution, the equations and boundary conditions are non-dimensionalized using the scales H (for x_i), H^{-1} (for κ_1 and κ_2), U_0 (for U), U_0/H (for ω_3), $\rho\nu a_0^2 U_0/H$ (for N_i), $\rho\nu a_0^4 U_0/H^2$ (for M_i) and ℓ (for s). The dimensionless arc length $\hat{s} = s/\ell \in [0, 1]$, as required by AUTO97. The resulting system of equations involves the two unknown parameters ℓ/H and $\Omega H/U_0$ and the three dimensionless groups $a_0/H \equiv \epsilon$ (slenderness), $gH^2/\nu U_0 \equiv B$ (gravity number) and $U_0 H/\nu \equiv Re$ (Reynolds number).

4. Scaling regimes

The motion of a coiling jet is controlled by the balance among viscous forces, gravity and inertia. Viscous forces arise from internal deformation of the jet by stretching (localized mainly in the tail) and by bending and twisting (mainly in the coil). Inertia includes the usual centrifugal and Coriolis accelerations, as well as terms proportional

to the along-axis rate of change of the magnitude and direction of the axial velocity $U\boldsymbol{d}_3$.

The coiling frequency is determined by the balance of forces in the coil itself, where the jet radius $a \approx a_1$ and the associated axial speed $U_1 \equiv Q/\pi a_1^2$ are nearly constant (figure 1a). To estimate the magnitudes of the forces in the coil, I use the torque-balance equation (2.14) to eliminate the shear stress resultants N_α from the force-balance equation (2.13). This yields

$$0 = \epsilon_{\alpha 3\beta}M_\beta'' + \rho A\epsilon_{\alpha 3\beta}\kappa_\beta U^2 - \rho gAd_{\alpha 3} + \cdots, \qquad (4.1)$$

where the ellipsis indicates additional terms that are of the same or higher order in the slenderness ϵ as those shown. The three terms in (4.1) represent the viscous force, inertia, and the gravitational force, respectively, all per unit length of the jet axis. Noting that $\mathrm{d}/\mathrm{d}s \sim \kappa_\beta \sim R^{-1}$ in the coil and using the constitutive relations (2.16b) and (2.16c) for M_β, one finds

$$\text{viscous force} \sim \rho\nu a_1^4 U_1 R^{-4}, \quad \text{gravitational force} \sim \rho g a_1^2, \quad \text{inertia} \sim \rho a_1^2 U_1^2 R^{-1}. \qquad (4.2)$$

Three different modes of coiling are possible, depending on how the viscous forces in the coil are balanced. The simplest case ('viscous' coiling) occurs when gravity and inertia are both negligible and the net viscous force acting on any element of fluid is zero. Coiling is here driven entirely by the injection of the fluid, like toothpaste squeezed from a tube. Because the jet deforms by bending and twisting with negligible stretching, its radius is nearly constant (figure 1b). Therefore, $a_1 \approx a_0$ and $U_1 \approx U_0$. Moreover, the fluid velocity is entirely controlled by the injection speed, and is independent of the jet's viscosity and radius. Dimensional considerations and the general relation $\Omega \sim U_1/R$ then imply

$$R \sim H \equiv R_{\mathrm{V}}, \qquad \Omega \sim a_1^{-2}QH^{-1} \equiv \Omega_{\mathrm{V}}. \qquad (4.3\,a)$$

A second mode, 'gravitational' coiling, occurs when viscous forces are balanced by gravity. The jet now comprises a long tapering tail and a coil that occupies only a small portion of the total height H (figure 1c). The scaling laws for this mode are

$$R \sim g^{-1/4}\nu^{1/4}Q^{1/4} \equiv R_{\mathrm{G}}, \qquad \Omega \sim g^{1/4}\nu^{-1/4}a_1^{-2}Q^{3/4} \equiv \Omega_{\mathrm{G}}. \qquad (4.3\,b)$$

A third mode, 'inertial' coiling, occurs when viscous forces in the coil are balanced by inertia (figure 1d). The scaling laws for inertial coiling are

$$R \sim \nu^{1/3}a_1^{4/3}Q^{-1/3} \equiv R_{\mathrm{I}}, \qquad \Omega \sim \nu^{-1/3}a_1^{-10/3}Q^{4/3} \equiv \Omega_{\mathrm{I}}, \qquad (4.3\,c)$$

and were first proposed by Mahadevan *et al.* (2000). It may at first sight seem contradictory that inertia can be important when the Reynolds number $Re = U_0H/\nu \ll 1$, as is the case for the jet shown in figure 1d ($Re = 0.031$). The paradox is resolved by noting that the effective Reynolds numbers in the coil and in the tail of the jet may be very different. Indeed, Re is an appropriate measure of the ratio of inertia to viscous forces only in the tail, and moreover only when U_1 does not greatly exceed U_0; then, inertia $\sim \rho a_0^2 U_0^2 H^{-1}$ and the viscous force $\sim \rho\nu a_0^2 U_0 H^{-2}$. In the coil itself, the magnitudes of inertia and the viscous force are given by (4.2), and the ratio of the two is of the order of unity in the inertial coiling regime defined by the scaling laws (4.3c). The physical reason for the larger role of inertia in the coil is that, for a
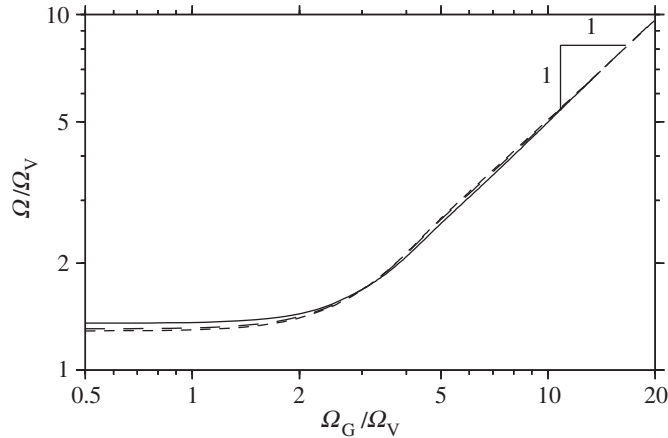
Figure 3. Scaling law for slow (inertia-free) coiling. Frequencies predicted by Auto97 are shown for $H/a_0 = 20$ (solid line), 40 (long-dashed line) and 80 (short-dashed line). Ω_V and Ω_G are defined by equations (4.3 a) and (4.3 b), respectively.

given strain rate, the viscous forces within a thin filament deformed by bending are much smaller than in one deformed by stretching.

I now demonstrate the existence of the three coiling modes by solving the full 17th-order boundary-value problem, using the numerical method described in § 3. Consider first the case of 'slow' coiling, which includes the two modes (viscous and gravitational) that involve no inertia. As the importance of gravity increases relative to the viscous forces—as the height of fall increases, for example—a transition from viscous to gravitational coiling will occur. The control parameter for this transition will be the ratio of the characteristic frequencies of the two modes, or $\Omega_G/\Omega_V \equiv H(g/\nu Q)^{1/4}$. Accordingly, a log–log plot of Ω/Ω_V versus Ω_G/Ω_V should define a universal curve with two distinct legs: one with zero slope corresponding to viscous coiling and another with unit slope corresponding to gravitational coiling. To test this, I used Auto97 to determine the coiling frequency as a function of the gravity number $gH^2/\nu U_0 \equiv B$ for three values of H/a_0, with all inertial terms suppressed ($Re \equiv U_0 H/\nu = 0$). For each solution, the jet radius a_1 was calculated as the average radius of those portions of the jet where the rate of energy dissipation due to stretching was less than 5% of the total. The scaled frequencies (figure 3) do in fact display the expected two-leg structure, with a transition from viscous to gravitational coiling occurring in the interval $2 < \Omega_G/\Omega_V < 3$. The three curves shown in figure 3 differ slightly because the jet axis at the contact point $s = \ell$ is at a small but finite height $a(\ell) \approx a_0$ above the plate (see figure 1b). A truly universal curve is obtained in the limit $H/a_0 \to \infty$, and is indistinguishable from the curve for $H/a_0 = 80$ in figure 3.

The effects of inertia are complex, and are best introduced via a direct comparison of numerical predictions with laboratory experiments. Mahadevan *et al.* (1998) measured the coiling frequency Ω and the jet radius a_1 for viscous silicone oil ($\nu = 1000 \text{ cm}^2 \text{ s}^{-1}$) by varying the fall height H with Q and a_0 fixed. Figure 4 shows curves of frequency versus height predicted numerically using Auto97 for the three pairs of values of Q and a_0 used by Mahadevan *et al.* (1998), together with the 15 frequencies they measured (open symbols). The experimental values of H, which
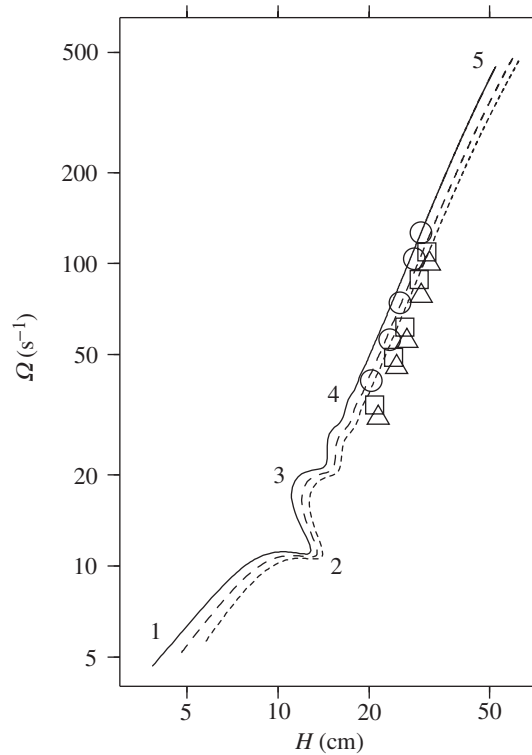
Figure 4. Coiling frequency versus fall height in the presence of inertia. Experimental measurements (open symbols) are shown for three series of experiments by Mahadevan *et al.* (1998) with viscous silicone oil ($\nu = 1000 \text{ cm}^2 \text{ s}^{-1}$) and $\{Q, a_0\} = \{0.57 \text{ cm}^3 \text{ s}^{-1}, 0.32 \text{ cm}\}$ (circles), $\{0.98 \text{ cm}^3 \text{ s}^{-1}, 0.40 \text{ cm}\}$ (squares) and $\{1.31 \text{ cm}^3 \text{ s}^{-1}, 0.48 \text{ cm}\}$ (triangles). The solid, dashed and dotted lines are the frequency–height curves predicted by Auto97 for the same three pairs of values of Q and a_0. Labels 1–5 denote reference points along the curves.

Mahadevan *et al.* (1998) did not report, were obtained by comparing the values of a_1 predicted by Auto97 with those measured by Mahadevan *et al.* (1998). The numerical predictions agree with the measured frequencies to within a root-mean-squared (RMS) error of 26%.

The most striking feature of the frequency–height curves in figure 4 is their multivaluedness in the height range 11–15 cm, where three coiling states with different frequencies are possible for the same values of a_0, H and Q. This complex structure reflects a transition from gravitational to inertial coiling as the fall height increases. Note first from (4.3 *b*) and (4.3 *c*) that the frequencies of gravitational and inertial coiling do not depend explicitly on the fall height H, but only on Q, a_1, ν and g. Standard dimensional analysis then implies that

$$\frac{\Omega}{\Omega_{\text{G}}} = F\left(\frac{\Omega_{\text{I}}}{\Omega_{\text{G}}}, \Pi\right), \quad \Pi = \frac{\nu}{g^{1/5} Q^{3/5}}, \tag{4.4}$$

where F is an unknown function to be determined. The first argument of F is the control parameter for the transition from gravitational to inertial coiling, while the second remains constant during an experiment in which the fall height (and hence a_1) varies.
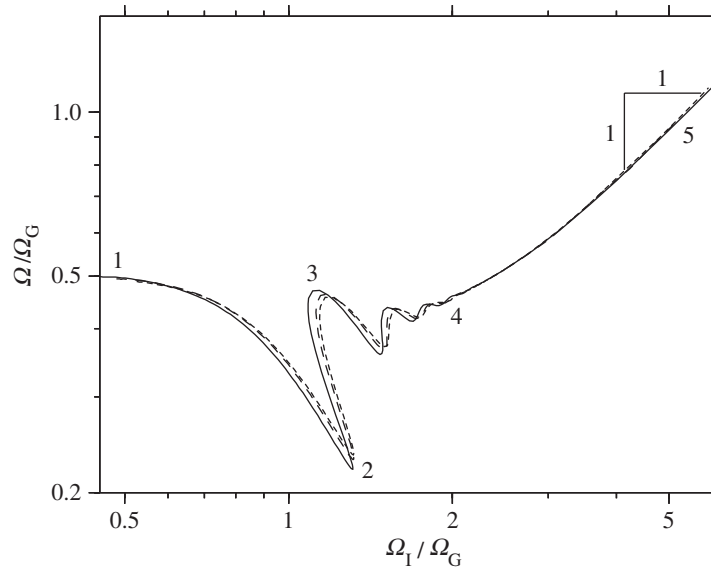
Figure 5. Transition from gravitational to inertial coiling in numerical solutions corresponding to the experiments of Mahadevan *et al.* (1998). Solid, dashed and dotted curves are rescaled versions of the same curves in figure 3. Values of $\Pi \equiv \nu/g^{1/5}Q^{3/5}$ for these three curves are 366, 265 and 223, respectively. The leftmost (zero slope) and rightmost (unit slope) limits of the curves correspond to purely gravitational and purely inertial coiling, respectively. Reference labels 1–5 are the same as in figure 4.

Figure 5 shows a log–log plot of Ω/Ω_G versus Ω_I/Ω_G for the numerical simulations of figure 4. The three curves coincide exactly at both the left and right limits of the plot, indicating scaling universality. On the left ($\Omega_I/\Omega_G \ll 1$), the curves approach a limit $\Omega = 0.49\Omega_G$ that corresponds to purely gravitational coiling, and which is identical to the rightmost portion of the curve in figure 3. At the far right of figure 5 ($\Omega_I/\Omega_G \gg 1$), the limiting form is $\Omega = 0.185\Omega_I$, corresponding to purely inertial coiling. In between is a complex transitional region in which both gravity and inertia are significant. In this region, Ω/Ω_G depends not only on Ω_I/Ω_G but also on Π, which ranges from 223 to 366 for the three curves shown. Between reference points 1 and 2, the coiling is dominantly gravitational, but its frequency is substantially reduced (up to a factor of 2.3) by inertia. Between points 2 and 3, the frequency is a strongly decreasing function of height (cf. figure 4), reflecting the increase of a_1 with height over this interval. At the end of the transitional region (point 4), the coiling is dominantly inertial, but its frequency is increased (by up to 25%) by gravity. The effect of gravity progressively diminishes until pure inertial coiling (unit slope in figure 5) is attained in the limit $\Omega_I/\Omega_G \gg 1$.

5. Dynamics of the tail

To this point, the jet radius a_1 in the coil has been treated as an independent variable. In reality, a_1 is controlled by the amount of gravity-induced stretching that occurs in the tail, and therefore depends on the external parameters (H, Q, a_0, ν and g) of the experiment. This dependence can be determined using a simple model for steady
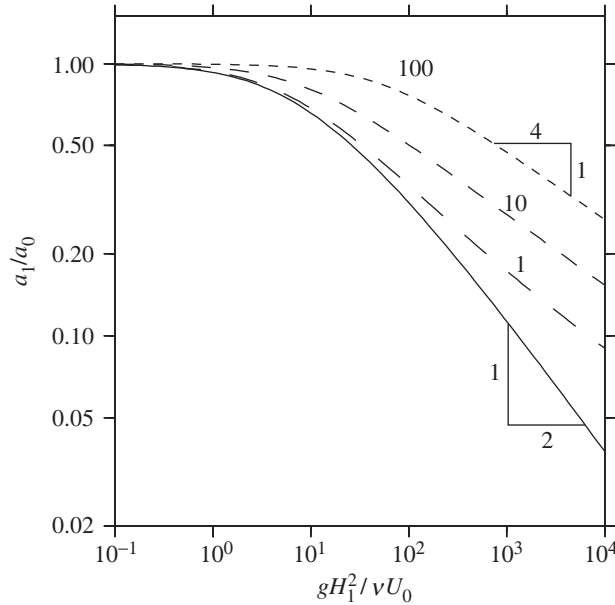
N. M. Ribe

Figure 6. Total thinning a_1/a_0 due to unidirectional stretching in the jet tail of length H_1. Portions of the curves with slope $-1/4$ correspond to free fall with negligible viscous resistance.

unidirectional stretching. The governing equation for this is just the $\boldsymbol{d}_3$-component of the global force-balance equation (2.13) with $\kappa_1 = \kappa_2 = x_1 = x_2 = 0$, or

$$3\nu U(U^{-1}U')' + g - UU' = 0. \tag{5.1}$$

The three terms in (5.1) represent the viscous resistance to stretching, gravity and inertia, respectively. The boundary conditions are

$$U(0) - U_0 = U'(H_1) = 0, \tag{5.2}$$

where the effective length $H_1 < H$ of the tail is defined by the point at which the stretching rate U' vanishes. I solved (5.1) and (5.2) numerically using a relaxation method (Press *et al.* 1996). Figure 6 shows $a_1/a_0 \equiv (U_0/U_1)^{1/2}$ as a function of the effective gravity number $B_1 = gH_1^2/\nu U_0$ and the Reynolds number $Re_1 = U_0H_1/\nu$. Gravity and inertia have opposite effects on thinning, enhancing and inhibiting it, respectively.

The solutions shown in figure 6 have simple analytical forms in two limiting cases. The first is $Re_1 = 0$, corresponding to a balance of gravity and viscous forces with negligible inertia. The solution for this case is

$$U = U_1 \cos^2\left[\left(\frac{2B_1U_0}{3U_1}\right)^{1/2}\left(\frac{s - H_1}{2H_1}\right)\right], \tag{5.3}$$

where U_1 satisfies the transcendental equation $U(0) = U_0$ that corresponds to the boundary condition at the injection point. In the limit $B_1 \to \infty$, the asymptotic expression for $a_1/a_0 \equiv (U_0/U_1)^{1/2}$ is

$$\frac{a_1}{a_0} = \frac{\sqrt{6}\pi}{2} B_1^{-1/2}[1 - \sqrt{6}B_1^{-1/2} + 6B_1^{-1} + O(B_1^{-3/2})]. \tag{5.4}$$

The second limit is $Re_1 B_1 \equiv gH_1^3/\nu^2 \to \infty$. Inertia now balances gravity everywhere except in thin boundary layers near the injection point and the lower end of the tail, and the solution is

$$\frac{a_1}{a_0} = \left(\frac{2gH_1}{U_0^2}\right)^{-1/4} \equiv \left(\frac{2B_1}{Re_1}\right)^{-1/4}. \tag{5.5}$$

This solution describes thinning by free fall with negligible injected kinetic energy, and corresponds to the portions of the curves with slope $-1/4$ in figure 6.

To compare the values of a_1/a_0 for the simple stretching model (figure 6) with those predicted by solutions of the complete 17th-order boundary-value problem, one needs to estimate the effective length H_1 of the tail in the latter solutions. I assume $H_1 = H - R$ as a simple approximation, but the results are hardly sensitive to the exact choice. The predictions of figure 6 then agree closely (RMS error 5%) with all the values of a_1/a_0 predicted by Auto97 that were used to construct figures 3–5.

6. Discussion

Fluid coiling has fundamental similarities with two related phenomena: periodic folding of viscous sheets and coiling of elastic ropes. Folding of viscous sheets is easily demonstrated in the home kitchen using honey, molten chocolate or cake batter, and may occur in the Earth's mantle when subducted oceanic lithosphere impinges on a boundary between layers with different viscosities and/or densities (Griffiths & Turner 1988). The two-dimensional flow within a folding sheet is simpler than that within a coiling filament, involving only two modes of deformation (stretching and bending) rather than four. On the other hand, folding, unlike coiling, is an essentially time-dependent phenomenon in which the motion of the contact line is both non-uniform and discontinuous. The folding of viscous sheets and filaments was studied by Skorobogatiy & Mahadevan (2000), who showed that experimentally measured folding frequencies of filaments confined to a plane obeyed a scaling law having the same form as the 'gravitational coiling' law $(4.3b)$. More recently, Ribe (2003) used a numerical model to show that a folding viscous sheet exhibits a transition from viscous to gravitational folding very similar to the one documented here (figure 3) for coiling.

Coiling of an elastic rope has been studied by Mahadevan & Keller (1996) (henceforth MK96), using a numerical model for a thin rope moving under the action of gravity, inertia and the elastic forces that resist bending. Because deformation by stretching and twisting is negligible in the rope, its coiling is described by a two-point boundary problem of order 13, compared with order 17 for fluid coiling. MK96 show that four modes of coiling are possible, depending on the values of the dimensionless parameters

$$F = \frac{U^2}{gH}, \qquad \gamma = \frac{\rho A g H^3}{EI}, \tag{6.1}$$

where U is the (constant) feeding velocity and E is the Young's modulus of the rope material. When $F = \gamma = 0$, both gravity and inertia are negligible, and the net elastic force on any element of the rope is zero (figure 1 of MK96). This case is analogous to the 'viscous' mode of fluid coiling. For $F \ll 1$ and $F\gamma \gg 1$, 'gravity-dominated' coiling occurs, in which the rope is nearly vertical over most of its length (the tail) and gravity balances elastic forces in the coil (figure $4b$ and leftmost portions of figures 2

and 3 of MK96). This case is therefore analogous to the 'gravitational' mode of fluid coiling. The two remaining modes, which MK96 call 'inertia-dominated' and 'inertia- and gravity-dominated', have no analogues in fluid coiling. In both cases, elastic forces are important only in small boundary layers near the feeding point and the plate, and most of the coil behaves as a perfectly flexible string in which axial tension is balanced by gravity and inertia. On the other hand, an elastic rope has no mode analogous to the inertial coiling of a fluid jet, in which inertia balances viscous resistance to bending in the coil.

A final important difference between elastic and fluid coiling is that the frequency of the former is always single valued, whereas three states of fluid coiling with different frequencies are possible for the same input parameters under certain conditions (cf. figures 3 and 4). But it is not guaranteed that all three of these solutions are stable. Theoretical analysis of this question would require a more general time-dependent theory for viscous jets, and is beyond the scope of this paper. However, recent experiments (Maleki *et al.* 2004) suggest that the solutions with the lowest and highest frequencies are stable, while the one with intermediate frequency (i.e. between reference points 2 and 3 in figures 3 and 4) is unstable.

While there is good agreement between the numerically predicted coiling frequencies and those measured by Mahadevan *et al.* (1998), further experimental confirmation of the numerical model is clearly needed. The most extensive experimental study of fluid coiling is that of Cruickshank (1980), who presented in graphical form some 700 measurements of the coiling frequency for different values of ν, a_0, Q and H. Regrettably, Cruickshank (1980) did not measure the critical parameter a_1, an oversight which reduces greatly the utility of his data. New experiments that demonstrate the existence of the three coiling modes identified here have now been performed, and will be reported separately (Maleki *et al.* 2004).

Appendix A. Global force and torque balance

A rigorous derivation of the governing equations for the flow within the jet requires the use of general nonorthogonal coordinates defined by the variable transformation (2.1). The general approach I follow here is that of Green & Zerna (1992), henceforth abbreviated as GZ. In this appendix, ∂_i denotes partial differentiation with respect to the variable y_i, where $y_3 \equiv s$.

Direct partial differentiation of (2.1) yields the covariant basis vectors

$$\boldsymbol{g}_1 \equiv \partial_1 \boldsymbol{r} = \boldsymbol{d}_1, \qquad \boldsymbol{g}_2 \equiv \partial_2 \boldsymbol{r} = \boldsymbol{d}_2, \qquad \boldsymbol{g}_3 \equiv \partial_3 \boldsymbol{r} = h\boldsymbol{d}_3 - \kappa_3(y_2\boldsymbol{d}_1 - y_1\boldsymbol{d}_2), \quad \text{(A 1)}$$

where

$$h \equiv \boldsymbol{g}_1 \cdot (\boldsymbol{g}_2 \times \boldsymbol{g}_3) = 1 - \kappa_2 y_1 + \kappa_1 y_2. \tag{A 2}$$

The associated contravariant (reciprocal) base vectors $\boldsymbol{g}^i$ satisfy $\boldsymbol{g}^i \cdot \boldsymbol{g}_j = \delta_j^i$, whence

$$\boldsymbol{g}^1 = \boldsymbol{d}_1 + h^{-1}\kappa_3 y_2 \boldsymbol{d}_3, \qquad \boldsymbol{g}^2 = \boldsymbol{d}_2 - h^{-1}\kappa_3 y_1 \boldsymbol{d}_3, \qquad \boldsymbol{g}^3 = h^{-1}\boldsymbol{d}_3. \tag{A 3}$$

The strain rate tensor within the jet is (GZ, p. 148)

$$e_{ij} = \tfrac{1}{2}(\boldsymbol{g}_i \cdot \partial_j \boldsymbol{u} + \boldsymbol{g}_j \cdot \partial_i \boldsymbol{u}). \tag{A 4}$$

Incompressibility of the fluid requires $g^{ij}e_{ij} = 0$ with $g^{ij} = \boldsymbol{g}^i \cdot \boldsymbol{g}^j$, or

$$\partial_1(hu_1) + \partial_2(hu_2) + \partial_3 u_3 + \kappa_3(y_2\partial_1 u_3 - y_1\partial_2 u_3) = 0. \tag{A 5}$$

The stress tensor relative to the local basis vectors $\boldsymbol{g}_i$ is

$$\tau^{ij} = -pg^{ij} + 2\mu g^{ik}g^{il}e_{kl}, \tag{A 6}$$

where p is the pressure. The equations of equilibrium are (GZ, p. 150)

$$h\rho\ddot{\boldsymbol{r}} = \partial_i(\sigma^{ij}\boldsymbol{d}_j) + h\rho\boldsymbol{f}, \tag{A 7}$$

where $\ddot{\boldsymbol{r}}$ is the acceleration and

$$\sigma^{ij} = \sigma_{ij} = h\tau^{ik}\boldsymbol{g}_k \cdot \boldsymbol{d}^j \tag{A 8}$$

is a modified (and non-symmetric) stress tensor relative to the axial basis vectors $\boldsymbol{d}^i \equiv \boldsymbol{d}_i$ and to a unit area of a reference surface at $y_1 = y_2 = 0$. Unlike τ^{ij}, σ_{ij} can meaningfully be integrated over cross-sections, because the basis vectors and the surface to which it is referred do not vary across the jet.

The equation for global force balance is obtained by integrating the momentum equations (A 7) over cross-sections of the jet and using the definitions (2.11) and (2.12) with $\boldsymbol{\sigma} = \sigma_{3i}\boldsymbol{d}_i$, yielding

$$\rho\int_S h\ddot{\boldsymbol{r}} = \boldsymbol{N}' + \rho A\boldsymbol{f}. \tag{A 9}$$

The equation for global torque balance is obtained by applying the operator $\boldsymbol{y} \times$ to (A 7) and then integrating, yielding

$$\rho\int_S h\boldsymbol{y} \times \ddot{\boldsymbol{r}} = \boldsymbol{M}' + \boldsymbol{d}_3 \times \boldsymbol{N} + \rho I[(\boldsymbol{f} \times \boldsymbol{d}_3)\boldsymbol{\kappa} - (\boldsymbol{\kappa} \times \boldsymbol{f})\boldsymbol{d}_3]. \tag{A 10}$$

The last term in (A 10), which represents a gravity-induced torque, is non-zero for the purely geometrical reason that the centre of gravity of an element of the jet does not lie on the axis if the jet is curved.

It remains only to evaluate the integrals on the left-hand sides of (A 9) and (A 10). To first order in y_1 and y_2, the acceleration associated with the velocity field (2.7) is

$$\begin{aligned}
\ddot{\boldsymbol{r}} = {}&\boldsymbol{\Omega} \times [\boldsymbol{\Omega} \times (\boldsymbol{x} + \boldsymbol{y})] + 2\boldsymbol{\Omega} \times \boldsymbol{u} \\
&+ U\boldsymbol{U}' + U\boldsymbol{\omega}' \times \boldsymbol{y} + (\boldsymbol{\kappa} \cdot \boldsymbol{y})\omega_3\boldsymbol{U} - \omega_3 U'\boldsymbol{d}_3 \times \boldsymbol{y} \\
&+ [(\boldsymbol{y} \times \boldsymbol{\kappa}) \cdot \boldsymbol{d}_3](U'\boldsymbol{U} - U\boldsymbol{\kappa} \times \boldsymbol{U}) - [\omega_3^2 + \tfrac{1}{2}UU'' - \tfrac{1}{4}(U')^2]\boldsymbol{y}.
\end{aligned} \tag{A 11}$$

The first two terms in the above expression are the usual centrifugal and Coriolis forces associated with the rotating reference frame, and the sum of the remaining terms is the acceleration of a particle measured in the rotating frame itself. The final forms (2.13) and (2.14) of the equations of global force and torque balance are obtained by substituting (A 11) into (A 9) and (A 10) and evaluating the integrals, after eliminating κ_3 using (2.10).

Appendix B. Constitutive relations

The constitutive relations (2.16) can be derived most simply by considering separately deformations dominated by stretching and by bending plus twisting. In all the expressions below, terms of higher order in the slenderness ϵ have been neglected.

For deformation dominated by stretching, the velocity within the jet is approximately

$$\boldsymbol{u} \sim U\boldsymbol{d}_3 - \tfrac{1}{2}U'\boldsymbol{y}. \tag{B 1}$$

The definition (A 8) then implies

$$\sigma_{33} \sim -p + 2\mu U', \qquad \sigma_{11} = \sigma_{22} \sim -p - \mu U', \tag{B 2}$$

where p is constant over the jet's cross-section. The vanishing of the normal stress at the jet's free surface requires $p = -\mu U'$, which implies $\sigma_{33} \sim 3\mu U'$. Substitution of this result into the definition (2.11) yields the constitutive relation (2.16 a).

For deformation dominated by bending and twisting, the velocity components u_1 and u_2 must be expanded to second order in the lateral coordinates y_α using the continuity equation (A 5). The resulting velocity field is

$$\boldsymbol{u} \sim U[1 - \kappa_2 y_1 + \kappa_1 y_2]\boldsymbol{d}_3 + \omega_3 \boldsymbol{d}_3 \times \boldsymbol{y}$$
$$+ (y_1^2 - y_2^2)(B_1\boldsymbol{d}_1 - B_2\boldsymbol{d}_2) + 2y_1 y_2 (B_2\boldsymbol{d}_1 + B_1\boldsymbol{d}_2), \tag{B 3}$$

where

$$B_\alpha = \tfrac{1}{4}[\epsilon_{\alpha\beta3}(U\kappa_\beta)' - \kappa_\alpha(\omega_3 - U\kappa_3)], \tag{B 4}$$

and terms proportional to the stretching rate U' (assumed negligible) have been ignored. The pressure varies linearly across the jet to lowest order, and can be written as

$$p = p_\alpha(s)y_\alpha. \tag{B 5}$$

The relevant components of the stress tensor σ_{ij} are now

$$\left.\begin{array}{l} \sigma_{3\alpha} \sim -\epsilon_{\alpha\beta3}\mu\omega_3' y_\beta, \\ \sigma_{33} \sim -(p_\alpha + 8\mu B_\alpha)y_\alpha, \\ \sigma_{11} = \sigma_{22} \sim -(p_\alpha - 4\mu B_\alpha)y_\alpha. \end{array}\right\} \tag{B 6}$$

The vanishing of the normal stress on the jet's free surface requires

$$p_\alpha = 4\mu B_\alpha. \tag{B 7}$$

Substitution of the above expressions into the definition (2.12) yields the constitutive relations (2.16 b)–(2.16 d). A more rigorous but lengthier derivation based on asymptotic expansions of the three-dimensional Navier–Stokes equations in powers of the slenderness ϵ (e.g. Ribe 2002) gives exactly the same results.

References

Barnes, G. & MacKenzie, J. 1959 Height of fall versus frequency in liquid rope-coil effect. *Am. J. Phys.* **27**, 112–115.

Barnes, G. & Woodcock, R. 1958 Liquid rope-coil effect. *Am. J. Phys.* **26**, 205–209.

Cruickshank, J. O. 1980 Viscous fluid buckling: a theoretical and experimental analysis with extensions to general fluid stability. PhD thesis, Iowa State University, Ames, IA, USA.

Cruickshank, J. O. 1988 Low-Reynolds-number instabilities in stagnating jet flows. *J. Fluid Mech.* **193**, 111–127.

Cruickshank, J. O. & Munson, B. R. 1981 Viscous fluid buckling of plane and axisymmetric jets. *J. Fluid Mech.* **113**, 221–239.

Doedel, E., Champneys, A. R., Fairgrieve, T. F., Kuznetsov, Y. A., Sandstede, B. & Wang, X. J. 2002 Auto97: continuation and bifurcation software for ordinary differential equations. (Available at http://indy.cs.concordia.ca/auto/.)

Entov, V. M. & Yarin, A. L. 1984 The dynamics of thin liquid jets in air. *J. Fluid Mech.* **140**, 91–111.

Green, A. E. & Zerna, W. 1992 *Theoretical elasticity.* New York: Dover.

Griffiths, R. W. & Turner, J. S. 1988 Folding of viscous plumes impinging on a density or viscosity interface. *Geophys. J.* **95**, 397–419.

Huppert, H. E. 1986 The intrusion of fluid mechanics into geology. *J. Fluid Mech.* **173**, 557–594.

Mahadevan, L. & Keller, J. B. 1996 Coiling of flexible ropes. *Proc. R. Soc. Lond.* A **452**, 1679–1694.

Mahadevan, L., Ryu, W. S. & Samuel, A. D. T. 1998 Fluid 'rope trick' investigated. *Nature* **392**, 140.

Mahadevan, L., Ryu, W. S. & Samuel, A. D. T. 2000 Correction: fluid 'rope trick' investigated. *Nature* **403**, 502.

Maleki, M., Habibi, M., Golestanian, R., Ribe, N. & Bonn, D. 2004 Liquid rope coiling. (Submitted.)

Pearson, J. R. A. 1985 *Mechanics of polymer processing.* Elsevier.

Press, W. H., Teukolsky, S. A., Vetterling, W. T. & Flannery, B. P. 1996 *Numerical recipes in* Fortran77*: the art of scientific computing*, 2nd edn. Cambridge University Press.

Ribe, N. M. 2002 A general theory for the dynamics of thin viscous sheets. *J. Fluid Mech.* **457**, 255–283.

Ribe, N. M. 2003 Periodic folding of viscous sheets. *Phys. Rev.* E **68**, 036305.

Skorobogatiy, M. & Mahadevan, L. 2000 Folding of viscous sheets and filaments. *Europhys. Lett.* **52**, 532–538.

Taylor, G. I. 1968 Instability of jets, threads, and sheets of viscous fluid. In *Proc. 12th Int. Cong. Applied Mechanics.* Springer.

Tchavdarov, B., Yarin, A. L. & Radev, S. 1993 Buckling of thin liquid jets. *J. Fluid Mech.* **253**, 593–615.

Tome, M. F. & McKee, S. 1999 Numerical simulation of viscous flow: buckling of planar jets. *Int. J. Numer. Meth. Fluids* **29**, 705–718.

Whittaker, E. T. 1944 *A treatise on the analytical dynamics of particles and rigid bodies*, 4th edn. New York: Dover.